Mesh-Based Autoencoders for Localized Deformation Component Analysis

Qingyang Tan,[1,2] Lin Gao,[1]* Yu-Kun Lai,[3] Jie Yang,[1,2] Shihong Xia[1]

[1]Beijing Key Laboratory of Mobile Computing and Pervasive Device,
Institute of Computing Technology, Chinese Academy of Sciences
[2]School of Computer and Control Engineering, University of Chinese Academy of Sciences
[3]School of Computer Science & Informatics, Cardiff University
tanqingyang14@mails.ucas.ac.cn, {gaolin, yangjie01, xsh}@ict.ac.cn, LaiY4@cardiff.ac.uk

Abstract

Spatially localized deformation components are very useful for shape analysis and synthesis in 3D geometry processing. Several methods have recently been developed, with an aim to extract intuitive and interpretable deformation components. However, these techniques suffer from fundamental limitations especially for meshes with noise or large-scale deformations, and may not always be able to identify important deformation components. In this paper we propose a novel mesh-based autoencoder architecture that is able to cope with meshes with irregular topology. We introduce sparse regularization in this framework, which along with convolutional operations, helps localize deformations. Our framework is capable of extracting localized deformation components from mesh data sets with large-scale deformations and is robust to noise. It also provides a nonlinear approach to reconstruction of meshes using the extracted basis, which is more effective than the current linear combination approach. Extensive experiments show that our method outperforms state-of-the-art methods in both qualitative and quantitative evaluations.

1 Introduction

With the development of 3D scanning and modeling technology, mesh data sets are becoming more and more popular. By analyzing these data sets with machine learning techniques, the latent knowledge can be exploited to advance geometry processing algorithms. In recent years, many research areas in geometry processing have benefited from this methodology, such as 3D shape deformation (Gao et al. 2016), 3D facial and human body reconstruction (Cao et al. 2015; Bogo et al. 2016), shape segmentation (Guo, Zou, and Chen 2015), etc. For shape deformation and human reconstruction, mesh sequences with different geometry and the same connectivity play a central role. Different geometric positions describe the appearance of the 3D mesh model while sharing the same vertex connectivity makes processing much more convenient. In such works, a key procedure is to build a low-dimensional control parametrization for the mesh data set, which provides a small set of intuitive parameters to control the generation of new shapes. For articulated models such as human bodies, the rigging method embeds a skeleton structure in the mesh to provide such a parametrization. However, the rigging operation is restrictive and does not generalize to other deformable shapes (e.g. faces). Parameterizing general mesh datasets which allows intuitive control in generating new shapes becomes an important and urgent research problem.

Early work extracted principal deformation components by using Principal Component Analysis (PCA) to reduce the dimensionality of the data set. However, such deformation components are global which do not lead to intuitive control. For example, when a user intends to deform the shape locally by specifying locally changed vertex positions as boundary conditions, the deformed shape tends to have unrelated areas deformed as well, due to the global nature of the basis. To address this, sparse localized deformation component (SPLOCS) extraction methods were recently proposed (Neumann et al. 2013; Huang et al. 2014; Wang et al. 2016). In these works the sparsity term is involved to localize deformation components within local support regions. However, these previous works suffer from different limitations: as we will show later, (Neumann et al. 2013; Huang et al. 2014) cannot handle large-scale deformations, and (Wang et al. 2016) is sensitive to noise which cannot extract the main deformation components robustly. We propose a novel mesh-based autoencoder architecture to extract meaningful local deformation components. We represent deformations of shapes in the dataset based on a recent effective representation (Gao et al. 2017) which is able to cope with large deformations. We then build a CNN-based autoencoder to transform the deformation representation to encoding in a latent space. Each convolutional layer involves convolutional operations defined on the mesh with arbitrary topology in the form of applying the same local filter to each vertex and its 1-ring neighbors, similar to (Duvenaud et al. 2015). We then introduce sparsity regularization to the weights in the fully-connected layers to promote identifying sparse localized deformations. The autoencoder structure ensures that the extracted deformation components are suitable for reconstructing high quality shape deformations.

Our main contributions are: 1) This is the first work that exploits CNN-based autoencoders for processing meshes with irregular connectivity. 2) Benefiting from sparse regularization and the nonlinear representation capability of autoencoders, our method is able to extract intuitive localized
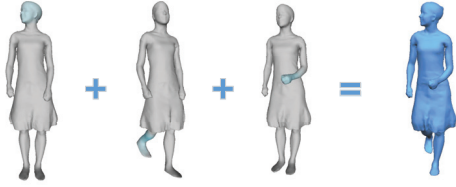

Figure 1: Synthesized model by combining deformation components derived from the Swing dataset (2008) using our method with equal weights.
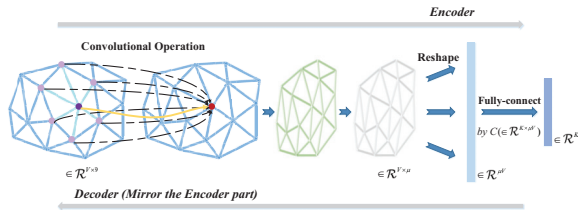

Figure 2: The proposed network architecture.

deformation components. It is able to deal with datasets with large-scale deformations, and is insensitive to noise. The method can extract important components even for challenging cases and generalizes well to reconstruction of unseen data. Extensive qualitative and quantitative experiments demonstrate that our method outperforms the state-of-the-art methods. We show an example of extracted deformation components (highlighted in blue) in Fig. 1, which are then combined to synthesize a novel, plausible shape. The architecture of our proposed network is illustrated in Fig. 2.

2 Related Work

Principal Deformation Components Analysis. With the increasing availability of 3D shapes, analyzing shape collections is becoming more important. Early work employs PCA to compress the mesh data set and extract global deformation components (Alexa and Muller 2000). The deformation components from the PCA are globally supported, which is not intuitive for shape editing and deformation, especially when the user wants to deform the shape locally in the spatial domain (Havaldar 2006). Sparse regularization is effective in localizing deformations (Gao, Zhang, and Lai 2012). However, standard sparse PCA (Zou, Hastie, and Tibshirani 2004) does not take spatial constraints into account and therefore the extracted deformation components do not aggregate in local spatial domains. By incorporating spatial constraints, a sparsity term is employed to extract localized deformation components (Neumann et al. 2013; Bernard et al. 2016), which performs better than region-based PCA variants (clustered PCA) (Tena, De la Torre, and Matthews 2011) in terms of extracting meaningful localized deformation components. However, it uses Euclidean coordinates which cannot represent shapes with large rotations. Later work addresses this limitation by using more advanced shape representations including deformation gradients (Huang et al. 2014) and edge and dihedral angle rep-

resentations (Wang et al. 2016). However, the former cannot cope with rotations larger than 180° which are very common in the animated mesh sequences, while the latter is not sensitive to the scale of the deformations which makes (Wang et al. 2016) not robust to noise. Unlike existing methods, we propose to exploit mesh-based autoencoders with sparse regularization along with an effective deformation representation (Gao et al. 2017) to extract high-quality deformation components, outperforming existing methods.

Neural Network Applications for 3D Shapes. Neural networks have achieved great success in different areas of computer science. Compared with 2D images, 3D shapes are more difficult to process, mainly due to their irregular connectivity and limited data availability. Nevertheless, some effort was made in recent years. For 3D object recognition, Su et al. (2015) and Shi et al. (2015) represent 3D shapes using multi-view projections or converting them to panoramic views and utilize 2D CNNs. Maturana and Scherer (2015) treat 3D shapes as voxels and extend 2D-CNNs to 3D-CNNs to recognize 3D objects. In addition, Li et al. (2015) analyze a joint embedding space of 2D images and 3D shapes. Tulsiani et al. (2016) abstract complex shapes using 3D volumetric primitives. For 3D shape synthesis, Wu et al. (2015) use deep belief networks to generate voxelized 3D shapes. Girdhar et al. (2016) combine an encoder for 2D images and a decoder for 3D models to reconstruct 3D shapes from 2D input. Yan et al. (2016) generate 3D models from 2D images by adding a projection layer from 3D to 2D. Choy et al. (2016) propose a novel recurrent network to map images of objects to 3D shapes. Sharma et al. (2016) train a volumetric autoencoder using noisy data with no labels for tasks such as denoising and completion. Wu et al. (2016) exploit the power of the generative adversarial network with a voxel CNN. In addition to voxel representation, Sinha et al. (2017) propose to combine ResNet and geometry images to synthesize 3D models. Li et al. (2017) and Nash and Williams (2017) propose to use neural networks for encoding and synthesizing 3D shapes based on pre-segmented data. All the methods above for synthesizing 3D models are restricted by their representations or primitives adopted, which are not suitable for analyzing and generating 3D motion sequences with rich details.

Convolutional Neural Networks (CNNs) on Arbitrary Graphs and Meshes. Traditional CNNs are defined on 2D images or 3D voxels with regular grids. Research has explored the potential to extend CNNs to irregular graphs by construction in the spectral domain (Bruna et al. 2013; Defferrard, Bresson, and Vandergheynst 2016) or the spatial domain (Niepert, Ahmed, and Kutzkov 2016; Duvenaud et al. 2015) focusing on spatial construction. Such representations are exploited in recent work (Boscaini et al. 2016; Yi et al. 2017) for finding correspondences or performing part-based segmentation on 3D shapes. Our method is based on spatial construction and utilizes this to build an autoencoder for analyzing deformation components.

3 Feature Representation

To represent large-scale deformations, we adapt a recently proposed deformation representation (Gao et al. 2017). Given a dataset with N shapes with the same topology, each shape is denoted as S_m, $m \in [1, \ldots, N]$. $\mathbf{p}_{m,i} \in \mathcal{R}^3$ is the ith vertex on the mth mesh model. The deformation gradient $\mathbf{T}_{m,i} \in \mathcal{R}^{3 \times 3}$ representing local shape deformations can be obtained by minimizing:

$$\underset{\mathbf{T}_{m,i}}{\arg \min} \sum_{j \in N(i)} c_{ij} \|(\mathbf{p}_{m,i} - \mathbf{p}_{m,j}) - \mathbf{T}_{m,i}(\mathbf{p}_{1,i} - \mathbf{p}_{1,j})\|_2^2.$$

where c_{ij} is the cotangent weight and $N(i)$ is the index set of 1-ring neighbors of the ith vertex. By polar decomposition $\mathbf{T}_{m,i} = \mathbf{R}_{m,i}\mathbf{S}_{m,i}$, the affine matrix $\mathbf{T}_{m,i} \in \mathcal{R}^{3 \times 3}$ can be decomposed into an orthogonal matrix $\mathbf{R}_{m,i}$ describing rotations, and a real symmetry matrix $\mathbf{S}_{m,i}$ for scale and shear deformations. The rotation matrix $\mathbf{R}_{m,i}$ can be rewritten as rotating around an axis $\boldsymbol{\omega}_{m,i}$ by an angle $\theta_{m,i}$. However, the mapping from the axis-angle representation to rigid rotation is surjective but not one to one: The rotation angles and axes in the set $\Omega_{m,i}$ correspond to one rigid rotation:

$$\Omega_{m,i} = \{(\boldsymbol{\omega}_{m,i}, \theta_{m,i} + t \cdot 2\pi), (-\boldsymbol{\omega}_{m,i}, -\theta_{m,i} + t \cdot 2\pi)\}$$

where t is an arbitrary integer. To overcome this, (Gao et al. 2017) proposes a novel representation to select the unique and consistent axis-angle representation by solving a global optimization to minimize the differences between adjacent rotation axes and angles.

For each vertex i of shape m, we obtain feature $q_{m,i} = \{r_{m,i}, s_{m,i}\} \in \mathcal{R}^9$ by extracting from matrices $\mathbf{R}_{m,i}$ and $\mathbf{S}_{m,i}$. To fit the scale of output activation function $tanh$ (explained later), we need to scale the feature values. Denote by $r_{m,i}^j$ and $s_{m,i}^j$ the jth dimension of $r_{m,i}$ and $s_{m,i}$ respectively. Separately for each dimension j, we linearly scale $r_{m,i}^j$ and $s_{m,i}^j$ from $[r_{min}, r_{max}]$ and $[s_{min}, s_{max}]$ to $[-0.95, 0.95]$ to acquire preprocessed $\widetilde{r_{m,i}^j}$ and $\widetilde{s_{m,i}^j}$, where $r_{min} = \min_{m,i,j} r_{m,i}^j$, and r_{max}, s_{min}, s_{max} are defined similarly. Then, we have $X_{m,i} = \{\widetilde{r_{m,i}}, \widetilde{s_{m,i}}\}$ as the deformation feature for vertex i of shape m.

4 Network Architecture

In this section, we present our framework including convolutional operations on irregular meshes, overall network structure, sparsity constraints and reconstruction loss.

Convolutional Operation

Our convolutional operation is extended from (Duvenaud et al. 2015) originally used for chemical molecules as a graph. In our representation, a mesh with irregular connectivity is the domain, and data vectors are associated with each vertex. For a convolutional layer, it takes input data $x \in \mathcal{R}^{V \times d}$, where V is the number of vertices, and d is the dimension of input data, and produces output data $y \in \mathcal{R}^{V \times d'}$ where d' is the dimension of the output data. Denote by x_i is the ith row of x corresponding to vertex i. Let its 1-ring neighbor

vertices be n_{ij} $j \in 1, 2, \ldots, D_i$, and D_i is the degree of vertex i. The convolutional operation is computed as:

$$y_i = W_{point}x_i + W_{neighbour}\frac{\sum_{j=1}^{D_i} x_{n_{ij}}}{D_i} + b, \quad (1)$$

where $W_{point}, W_{neighbour} \in \mathcal{R}^{d' \times d}$ are weights for the convolutional operation, and $b \in \mathcal{R}^{d'}$ is the bias of the layer.

Network Structure

The overall network is built based on the convolutional operation and with an autoencoder structure. The input to the encoder part is preprocessed features which are shaped as $X \in \mathcal{R}^{V \times 9}$, where 9 is the dimension of the deformation representation. Then we stack several convolutional layers with $tanh$ as the output activation function. We tested alternative functions like $ReLU$, but they performed worse in the quantitative analysis. The number of layers and the dimension of each layer are dependent on V and model numbers for different datasets. If the encoder part has more than one convolutional layer, the last convolutional layer will directly use linear output without any non-linear activation function to avoid overfitting. The output from the last convolutional layer is reshaped as a vector $f \in \mathcal{R}^{\mu V}$, where μ is the output dimension of the last convolutional layer. We use $C \in \mathcal{R}^{K \times \mu V}$ to map the feature to the latent space $z \in \mathcal{R}^K$ where K is the dimension of the latent space:

$$z = Cf. \quad (2)$$

To reconstruct the shape representation from z, we use the decoder, which basically mirrors the encoder steps. We first use the transpose of C to transfer from the latent space back to the feature space:

$$\widehat{f} = C^T z. \quad (3)$$

For the decoder convolutional layers, we use the transposed weights of the corresponding layer in the encoder, with all layers using the $tanh$ output activation function. The output of the whole network is $\widehat{X} \in \mathcal{R}^{V \times 9}$ which has the identical dimension as the input and can be scaled back to the deformation representation (Gao et al. 2017) and used for reconstructing the deformed shape.

The tied weight formulation of the autoencoder makes it more like PCA, and we assume that $F \in \mathcal{R}^{N \times \mu V}$ is assembled by stacking all the features f extracted from the last convolutional layer for N models in the dataset. Then, C can be seen as K deformation components of F, and $Z \in \mathcal{R}^{N \times K}$ stacks the latent representations of the N models in the dataset, which is treated as combinational weights to reconstruct the shape.

Sparsity Constraints and Reconstruction Loss

Following the idea from (Neumann et al. 2013), we use group sparsity ($\ell_{2,1}$ norm) to urge deformation components to only capture local deformations. The constraints are added on C as:

$$\Omega(C) = \frac{1}{K} \sum_{k=1}^{K} \sum_{i=1}^{V} \Lambda_{ik} \|C_k^i\|_2, \quad (4)$$
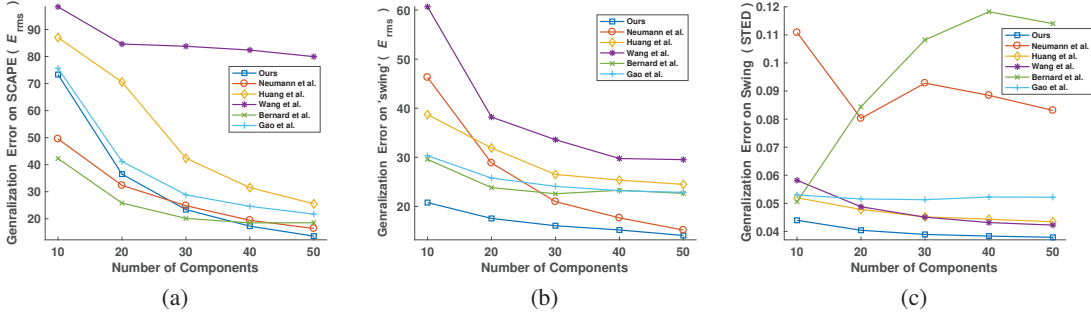
Figure 3: Errors of applying our model to generate unseen data, using (a) SCAPE (Anguelov et al. 2005), (b) (c) Swing (Vlasic et al. 2008) datasets. We use metrics E_{rms} and STED with different component numbers. Our method outperforms other methods in all datasets and metrics even for limited training data.

Dataset	Metric	Method				
		Ours	Wang et al.	Huang et al.	Neumann et al.	Bernard et al.
Horse	E_{rms}	12.9605	29.6090	18.0624	**7.3682**	20.1994
	$STED$	**0.04004**	0.04332	0.05273	0.08074	0.4111
Face	E_{rms}	**2.9083**	8.5620	12.3221	2.9106	2.9853
	$STED$	**0.007344**	0.01320	0.01827	0.008611	0.02662
Jumping	E_{rms}	**24.4827**	44.3362	37.9915	29.3368	49.9374
	$STED$	**0.04862**	0.05400	0.06305	0.1268	0.4308
Humanoid	E_{rms}	**3.4912**	60.9925	16.1995	14.3610	6.6320
	$STED$	**0.01313**	0.03757	0.02247	0.07319	0.04612

Table 1: Errors of applying our method to generate unseen data from Horse (Sumner and Popović 2004), Face (Zhang et al. 2004), Jumping (Vlasic et al. 2008) and Humanoid datasets. We train all these methods with 50 components.

where C_k^i is the μ-dimensional vector associated with component k of vertex i, and Λ_{ik} is sparsity regularization parameters based on normalized geodesic distances:

$$\Lambda_{ik} = \begin{cases} 0 & d_{ik} < d_{min} \\ 1 & d_{ik} > d_{max} \\ \frac{d_{ik} - d_{min}}{d_{max} - d_{min}} & \text{otherwise.} \end{cases} \quad (5)$$

d_{ik} denotes the normalized geodesic distance from vertex i to the center point c_k of component k which is defined as:

$$c_k = \operatorname*{argmax}_i \|C_k^i\|_2. \quad (6)$$

c_k will be updated after optimizing C in each iteration. Intuitively, Λ maps a geodesic distance to the range of $[0, 1]$ with distances out of the range of $[d_{min}, d_{max}]$ capped. d_{min} and d_{max} are two tunable parameters, and control the size of deformation region of one component. For most datasets, we use $d_{min} = 0.2$ and $d_{max} = 0.4$. To fit the training process of neural network, we precomputed all the geodesic distances between two vertices using (Crane, Weischedel, and Wardetzky 2013), which are then normalized by the largest pairwise geodesic distance.

Since $C^T Z = (\frac{C^T}{\alpha})(\alpha Z) \quad \forall \alpha \neq 0$, to avoid trivial solutions with arbitrarily small C values and arbitrary large Z values, we also add constraints to Z as a regularization term:

$$\mathcal{V}(Z) = \frac{1}{K} \sum_{j=1}^{K} (\max_m |Z_{jm}| - \theta), \quad (7)$$

where Z_{jm} is the jth dimension of model m's weight, and θ is a small positive number. We set $\theta = 5$ in all the experiments. We use Mean Square Error (MSE) to urge the network to reconstruct the representation of models, and the total loss function is:

$$\mathcal{L} = \frac{1}{N} \sum_{m=1}^{N} \|\widehat{X}_m - X_m\|_2^2 + \lambda_1 \Omega(C) + \lambda_2 \mathcal{V}(Z), \quad (8)$$

where $\widehat{X}_m$ and X_m are input and output of model m (data term), $\Omega(C)$ is the sparse localized regularization. We set $\lambda_1 = \lambda_2 = 0.5$ in all the experiments. The whole network pipeline is illustrated in Fig. 2. We use ADAM algorithm (Kingma and Ba 2015) and set the learning rate to be 0.001 to train the network.

5 Applications
Once trained, the network can be used to perform many useful tasks, including dimensionality reduction, reconstruction, component analysis and shape synthesis. The first two
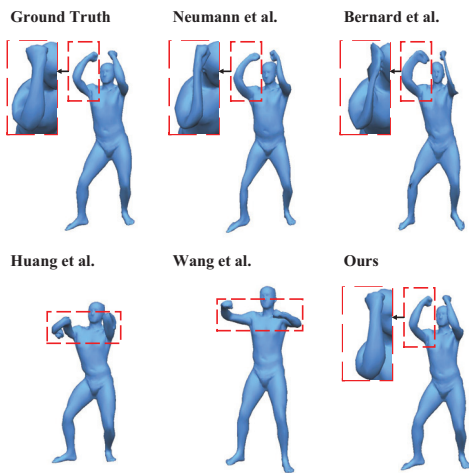
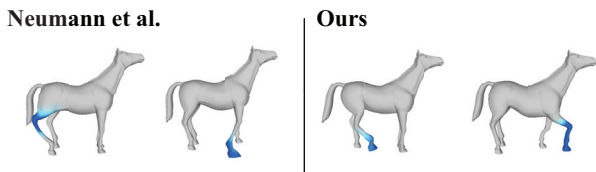Figure 4: Visual comparison of reconstruction results of the SCAPE dataset (2005).

Figure 5: Components of horse dataset (2004) extracted by (Neumann et al. 2013) and our method.

applications are straightforward, so we now give details for performing the last two applications.

Component Analysis

The matrix C corresponds to the localized deformation components. We assume the rth model is the reference model (which can be the first model in the dataset) which has a latent vector Z_r. To analyze the ith deformation component, we calculate the minimum and maximum values of the ith dimension of the embedding, denoted by $Z_{i_{min}} = \min_m Z_{i,m}$ and $Z_{i_{max}} = \max_m Z_{i,m}$. We can then obtain latent vectors $\widehat{Z}_{i_{min}}$ and $\widehat{Z}_{i_{max}}$ corresponding to the two extreme values of the ith component by replacing the ith component of Z_r with $Z_{i_{min}}$ and $Z_{i_{max}}$, respectively. Applying the vectors to the decoder produces the output mesh features $\widehat{X_{min}}$ and $\widehat{X_{max}}$. We work out the differences $\|\widehat{X_{min}} - X_r\|$ and $\|\widehat{X_{max}} - X_r\|$ and the one that has larger distance from the reference model X_r is chosen as the representative shape for the ith deformation component, with the corresponding latent vector denoted as Z_{i_h}. The displacement of each vertex feature indicates the strength of the deformation, which can be visualized to highlight changed positions.

Shape Synthesis

To synthesize new models, the user can specify a synthesis weight w_{s_i} for the ith deformation component, and the de-

formed shape in the latent space can be obtained as:

$$z_{si} = Z_{ir} + (Z_{ih} - Z_{ir}) \times w_{si}, \tag{9}$$

where z_{si} represents the ith dimension of obtained weight z_s in the latent space. Then, by feeding z_s in as input to the decoder, the synthesized model feature can be obtained which can be used for reconstructing the synthesized shape.

6 Experimental Results

Quantitative Evaluation

We compare the generalization ability of our method with several state-of-the-art methods, including original SPLOCS (Neumann et al. 2013), SPLOCS with deformation gradients (Huang et al. 2014), SPLOCS with edge lengths and dihedral angles (Wang et al. 2016), SPLOCS with the feature from (Gao et al. 2017) as used in this paper, and (Bernard et al. 2016). We use SCAPE (Anguelov et al. 2005) and Swing (Vlasic et al. 2008) datasets to conduct main quantitative evaluation.

For the SCAPE dataset, we randomly choose 36 models as the training set and the remaining 35 models as the test set. After training, we compare the generalization error on the test set with different methods, using E_{rms} (root mean square) error (Kavan, Sloan, and O'Sullivan 2010). The results are shown in Fig. 3(a). Fig. 4 shows the visual comparison of reconstruction results. For the Swing dataset, we randomly select one model from every ten models for training (15 models) and remaining for testing (135 models). We compare E_{rms} error as well as $STED$ error (Vasa and Skala 2011) designed for motion sequences with a focus on 'perceptual' error of models. The results are shown in Figs. 3(b) and 3(c). Note that since the vertex position representation cannot handle rotations well, the more components methods (Neumann et al. 2013; Bernard et al. 2016) use, the more artifacts would be brought in the reconstructed models, thus $STED$ error may increase with more components. The results indicate that our method has better quantitative reconstruction results than other methods, with lower reconstruction errors when sufficient components are used. From the visual results, we can see that (Neumann et al. 2013; Bernard et al. 2016; Huang et al. 2014) cannot handle large-scale rotations well and cannot reconstruct plausible models in such cases, while (Wang et al. 2016) can be affected by noise in the dataset and cannot recover some actions precisely. Our method does not have such drawbacks. Comparison with SPLOCS using (Gao et al. 2017) demonstrates that our autoencoder is effective, beyond the benefits from the representation. We also experiment using linearly combined components derived from our method to reconstruct unseen models, and the errors of SPLOCS with (Gao et al. 2017) are greater than our non-linear framework. For example, for the Swing dataset with 50 components, the E_{rms} error is 25.2994, and $STED$ error is 0.05214 (whereas for our method these two errors are 14.0836 and 0.03789). For the SCAPE dataset, the E_{rms} error is 17.1754, which is larger than our error 13.556. This shows that our non-linear method can find intrinsic patterns and better fit the relationships between the latent space and feature domain.
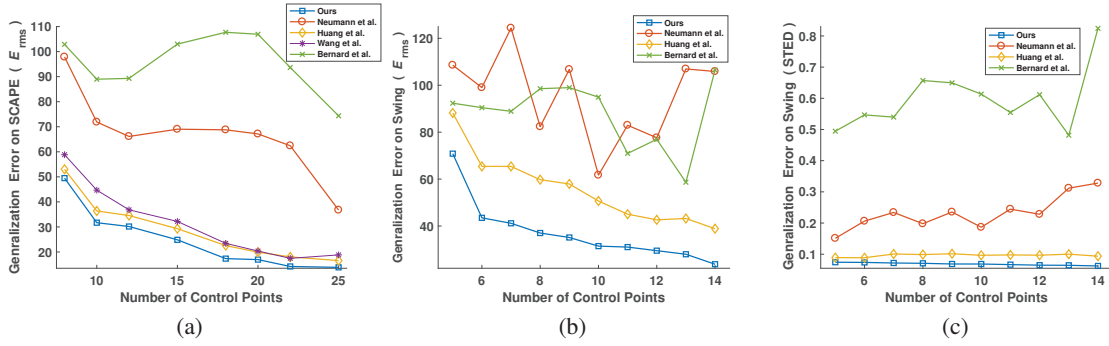
Figure 6: We use limited control points to reconstruct unseen data in the SCAPE (Anguelov et al. 2005) and Swing (Vlasic et al. 2008) datasets, and report the generalization errors.
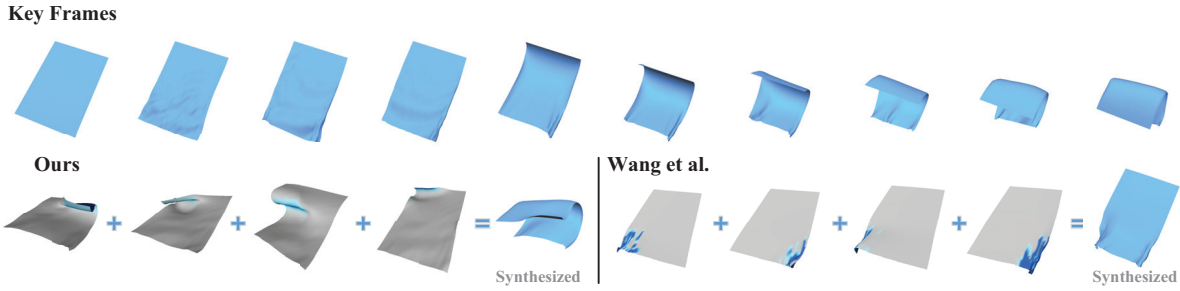

Figure 7: Top row: key frames of a flag dataset we created through physical simulation. Bottom row: and the first four deformation components extracted by our method and (Wang et al. 2016). We also present the synthesis results by combining the four components with equal weights, which shows our result is more plausible.

The major parameters in our method are λ_1 and λ_2, which are used for balancing regularization terms. For all the experiments, we set them to 0.5. To verify the sensitivity of our method with these two parameters, we perform additional experiments to compare results when we change them in the range of 0.4–0.6, and it does not greatly affect quantitative performance. An example is shown in Table 2, which is performed on the SCAPE dataset with 50 components.

Following the previous experiment, 50 components are generally sufficient to fit data well for all the methods, which are therefore used in the following comparative experiments. The results are summarized in Table 1. All the datasets we use here can be seen as motion sequences, so we use the same training-test split used for the Swing dataset, and use the two metrics to evaluate errors. Although for the Horse dataset (Sumner et al. 2005), the method (Neumann et al. 2013) has a lower E_{rms} error than our method, their method cannot cope with such dataset with large deformations and suffers from artifacts. The components extracted by our method and (Neumann et al. 2013) are shown in Fig. 5.

Meanwhile, to quantitatively compare the sparse control ability of these methods, we randomly select a few points on the mesh and test the ability of each method to recover the whole mesh through these limited points. This situation is similar to the scenario that users put limited control points on significant joints to acquire models with meaningful actions. To obtain control points evenly distributed on the mesh

(λ_1, λ_2)	$(0.4, 0.4)$	$(0.6, 0.6)$	$(0.4, 0.6)$	$(0.6, 0.4)$
E_{rms}	14.1763	13.6429	14.2645	14.093

Table 2: Reconstruction error for unseen data from SCAPE (Anguelov et al. 2005) when different λ_1 and λ_2 are used. The default values are both 0.5, and the error is 13.556.

surface, we randomly choose the first point, and then use Voronoi sampling to acquire the other points. We test the results on SCAPE and Swing datasets. For both methods, we choose 50 components, and for (Neumann et al. 2013) and (Bernard et al. 2016), we solve the reconstruction problem directly using the limited points, while for the other methods, we use data-driven deformation with the extracted components. The results in Fig. 6 show that our method performs well, consistently with smallest errors in both metrics. The datasets we use in this experiment contain a great amount of rotation. Therefore, using limited control points may not allow the components extracted by (Neumann et al. 2013) and (Bernard et al. 2016) to recover the whole mesh, resulting in large fluctuations in the error curves.

Qualitative Evaluation

Flag Dataset. To verify our method's ability to capture primary deformation components even when there is signifi-
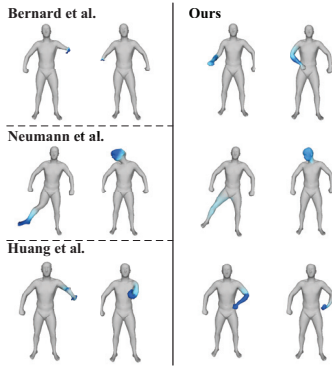
Figure 8: Comparison of deformation components located in similar areas, which are extracted by different methods.
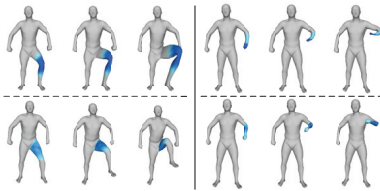

Figure 9: Synthesis results with different components of the SCAPE dataset (2005): The left group contains the components about lifting the left leg extracted by Neumann et al. (first row) and our method (second row) with weights 0.5, 1.0 and 1.5. The right group contains the components about lifting the left arm extracted by Huang et al. (first row) and our method (second row) with weights 0.3, 0.6 and 0.9.

cant noise, we test on a flag dataset created by physical simulation and compare our method with (Wang et al. 2016). For both methods, we extract 20 components, and the first four components along with the key frames of the dataset are shown in Fig. 7. Our method is able to extract the main movements (large-scale swinging of the flag), and separate local movements in the left and right parts of the flag. The synthesized result with the four components is reasonable. However, (Wang et al. 2016) only captures the noise around the corner of flags, and the reconstructed shape does not capture the true deformation.
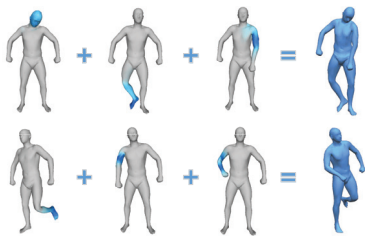

Figure 10: Synthesized models based on components derived from SCAPE dataset (2005) by our method.
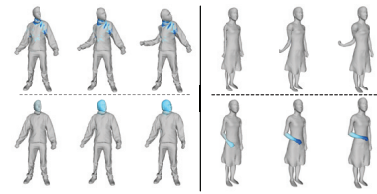

Figure 11: Synthesis results with components of Jumping and Swing datasets (2008): The left group contains the components about shaking head extracted by Wang et al. (first row) and our method (second row) with weights 0.4, 0.8 and 1.2. The right group contains the components about lifting the right arm extracted by Wang et al. (first row) and our method (second row) with weights 0.6, 0.9 and 1.2.

SCAPE Dataset. We compare our results on the SCAPE dataset with (Neumann et al. 2013; Huang et al. 2014; Bernard et al. 2016). The corresponding components extracted by our method and the other methods are shown in Fig. 8, and two groups of components about lifting the left leg (extracted by our method and Neumann et al.) and left arm (extracted by our method and Huang et al.) with different weights are shown in Fig. 9. These justify that our method can handle large-scale rotation better than the other methods without artifacts like irrational amplification and shrinkage. Our proposed method also has powerful synthesis ability. We show synthesis results by combining several different deformation components in Fig. 10.

Swing and Jumping Datasets. For Swing and Jumping datasets from (Vlasic et al. 2008), we align all the models and then train the network. The synthesis results of our method are compared with those of (Wang et al. 2016) in Fig. 11. The first group of components are about shaking head to left from the Jumping dataset. Our method focuses on the movement of the head and can produce reasonable models, while models generated by (Wang et al. 2016) are disturbed by the clothes, and have artifacts of arm structure. The second group of models are about lifting the left arms from the Swing dataset, (Wang et al. 2016) even finds wrong direction for this movement. We show synthesis results by combining three different components in Fig. 1.

7 Conclusion

In this paper, we propose a novel CNN based autoencoder on meshes to extract localized deformation components. Extensive quantitative and qualitative evaluations show that our method is effective, outperforming state-of-the-art methods.

8 Acknowledgments

References

Alexa, M., and Muller, W. 2000. Representing Animations by Principal Components. *Comp. Graph. Forum*.

Anguelov, D.; Srinivasan, P.; Koller, D.; Thrun, S.; Rodgers, J.; and Davis, J. 2005. SCAPE: shape completion and animation of people. *ACM Trans. Graph.* 24(3):408–416.

Bernard, F.; Gemmar, P.; Hertel, F.; Goncalves, J.; and Thunberg, J. 2016. Linear shape deformation models with local support using graph-based structured matrix factorisation. In *CVPR*, 5629–5638.

Bogo, F.; Kanazawa, A.; Lassner, C.; Gehler, P.; Romero, J.; and Black, M. J. 2016. Keep it SMPL: Automatic estimation of 3D human pose and shape from a single image. In *ECCV*.

Boscaini, D.; Masci, J.; Rodolà, E.; Bronstein, M. M.; and Cremers, D. 2016. Anisotropic diffusion descriptors. In *Comp. Graph. Forum*, volume 35, 431–441.

Bruna, J.; Zaremba, W.; Szlam, A.; and LeCun, Y. 2013. Spectral networks and locally connected networks on graphs. *arXiv:1312.6203*.

Cao, C.; Bradley, D.; Zhou, K.; and Beeler, T. 2015. Real-time high-fidelity facial performance capture. *ACM Trans. Graph.* 34(4):46.

Choy, C. B.; Xu, D.; Gwak, J.; Chen, K.; and Savarese, S. 2016. 3D-R2N2: A unified approach for single and multi-view 3D object reconstruction. In *ECCV*, 628–644.

Crane, K.; Weischedel, C.; and Wardetzky, M. 2013. Geodesics in Heat: A New Approach to Computing Distance Based on Heat Flow. *ACM Trans. Graph.* 32.

Defferrard, M.; Bresson, X.; and Vandergheynst, P. 2016. Convolutional neural networks on graphs with fast localized spectral filtering. In *NIPS*, 3844–3852.

Duvenaud, D. K.; Maclaurin, D.; Iparraguirre, J.; Bombarell, R.; Hirzel, T.; Aspuru-Guzik, A.; and Adams, R. P. 2015. Convolutional networks on graphs for learning molecular fingerprints. In *NIPS*, 2224–2232.

Gao, L.; Lai, Y.-K.; Liang, D.; Chen, S.-Y.; and Xia, S. 2016. Efficient and flexible deformation representation for data-driven surface modeling. *ACM Trans. Graph.* 35(5):158.

Gao, L.; Lai, Y.-K.; Yang, J.; Zhang, L.-X.; Kobbelt, L.; and Xia, S. 2017. Sparse Data Driven Mesh Deformation. *arXiv:1709.01250*.

Gao, L.; Zhang, G.; and Lai, Y. 2012. Lp shape deformation. *Science China Information Sciences* 55(5):983–993.

Girdhar, R.; Fouhey, D.; Rodriguez, M.; and Gupta, A. 2016. Learning a predictable and generative vector representation for objects. In *ECCV*.

Guo, K.; Zou, D.; and Chen, X. 2015. 3D mesh labeling via deep convolutional neural networks. *ACM Trans. Graph.* 35(1):3.

Havaldar, P. 2006. Performance driven facial animation. In *ACM SIGGRAPH 2006 Course 30 Notes*.

Huang, Z.; Yao, J.; Zhong, Z.; Liu, Y.; and Guo, X. 2014. Sparse localized decomposition of deformation gradients. *Comp. Graph. Forum* 33(7):239–248.

Kavan, L.; Sloan, P.-P.; and O'Sullivan, C. 2010. Fast and efficient skinning of animated meshes. *Comp. Graph. Forum* 29(2):327–336.

Kingma, D., and Ba, J. 2015. ADAM: A method for stochastic optimization. In *ICLR*.

Li, Y.; Su, H.; Qi, C. R.; Fish, N.; Cohen-Or, D.; and Guibas, L. J. 2015. Joint embeddings of shapes and images via cnn image purification. *ACM Trans. Graph.* 34(6):234.

Li, J.; Xu, K.; Chaudhuri, S.; Yumer, E.; Zhang, H.; and Guibas, L. 2017. Grass: Generative recursive autoencoders for shape structures. *ACM Trans. Graph.* 36(4).

Maturana, D., and Scherer, S. 2015. Voxnet: a 3D convolutional neural network for real-time object recognition. In *IEEE Conference on Intelligent Robots and Systems*, 922–928.

Nash, C., and Williams, C. K. 2017. The shape variational autoencoder: A deep generative model of part-segmented 3D objects. *Comp. Graph. Forum*.

Neumann, T.; Varanasi, K.; Wenger, S.; Wacker, M.; Magnor, M.; and Theobalt, C. 2013. Sparse localized deformation components. *ACM Trans. Graph.* 32(6):179.

Niepert, M.; Ahmed, M.; and Kutzkov, K. 2016. Learning convolutional neural networks for graphs. In *ICML*, 2014–2023.

Sharma, A.; Grau, O.; and Fritz, M. 2016. Vconv-dae: Deep volumetric shape learning without object labels. In *ECCV Workshops*, 236–250.

Shi, B.; Bai, S.; Zhou, Z.; and Bai, X. 2015. Deeppano: Deep panoramic representation for 3-d shape recognition. *IEEE Signal Processing Letters* 22(12):2339–2343.

Sinha, A.; Unmesh, A.; Huang, Q.; and Ramani, K. 2017. SurfNet: Generating 3D shape surfaces using deep residual networks. In *CVPR*.

Su, H.; Maji, S.; Kalogerakis, E.; and Learned-Miller, E. 2015. Multi-view convolutional neural networks for 3D shape recognition. In *IEEE ICCV*, 945–953.

Sumner, R. W., and Popović, J. 2004. Deformation transfer for triangle meshes. *ACM Trans. Graph.* 23(3):399–405.

Sumner, R. W.; Zwicker, M.; Gotsman, C.; and Popović, J. 2005. Mesh-based inverse kinematics. *ACM Trans. Graph.* 24(3):488–495.

Tena, J. R.; De la Torre, F.; and Matthews, I. 2011. Interactive region-based linear 3D face models. *ACM Trans. Graph.* 30(4):76.

Tulsiani, S.; Su, H.; Guibas, L. J.; Efros, A. A.; and Malik, J. 2016. Learning shape abstractions by assembling volumetric primitives. *arXiv:1612.00404*.

Vasa, L., and Skala, V. 2011. A perception correlated comparison method for dynamic meshes. *IEEE Trans. Vis. Comp. Graph.* 17(2):220–230.

Vlasic, D.; Baran, I.; Matusik, W.; and Popović, J. 2008. Articulated mesh animation from multi-view silhouettes. *ACM Trans. Graph.* 27(3):97.

Wang, Y.; Li, G.; Zeng, Z.; and He, H. 2016. Articulated-motion-aware sparse localized decomposition. *Comp. Graph. Forum*.

Wu, Z.; Song, S.; Khosla, A.; Yu, F.; Zhang, L.; Tang, X.; and Xiao, J. 2015. 3D ShapeNets: A deep representation for volumetric shapes. In *CVPR*, 1912–1920.

Wu, J.; Zhang, C.; Xue, T.; Freeman, W. T.; and Tenenbaum, J. B. 2016. Learning a probabilistic latent space of object shapes via 3D generative-adversarial modeling. In *NIPS*, 82–90.

Yan, X.; Yang, J.; Yumer, E.; Guo, Y.; and Lee, H. 2016. Perspective transformer nets: Learning single-view 3d object reconstruction without 3d supervision. In *NIPS*. 1696–1704.

Yi, L.; Su, H.; Guo, X.; and Guibas, L. J. 2017. SyncSpecCNN: Synchronized spectral CNN for 3D shape segmentation. In *CVPR*.

Zhang, L.; Snavely, N.; Curless, B.; and Seitz, S. M. 2004. Space-time faces: High-resolution capture for modeling and animation. In *ACM SIGGRAPH*, 548–558.

Zou, H.; Hastie, T.; and Tibshirani, R. 2004. Sparse principal component analysis. *J. Comp. Graph. Statistics* 15:2006.